11

Ti-based Bulk Metallic Glasses for Biomedical Applications

Fengxiang Qin, Zhenhua Dan, Xinmin Wang, Guoqiang Xie and Akihisa Inoue
Institute for Materials Research, Tohoku University, Japan

1. Introduction

Biomedical materials can improve the life quality of a number of people each year. The range of applications includes such as joint and limb replacements, artificial arteries and skin, contact lenses, and dentures. So far the accepted biomaterials include metals, ceramics and polymers. The metallic biomaterials mainly contain stainless steel, Co-Cr alloys, Titanium and Ti-6Al-4V. Recently, bulk metallic glasses as novel materials have been rapidly developed for the past two decades in Mg-, Ln-, Zr-, Fe-, Ti-, Pd-, Cu-, Ni-based alloy systems because of their unique physical, chemical, magnetic and mechanical properties compared with conventional crystalline alloys. Metallic glass formation is achieved by avoiding nucleation and growth of crystalline phases when cooling the alloy from the molten liquid. Therefore, the different atomic configurations induced significantly different characteristic features such as high strength, good corrosion resistance and excellent electromagnetic properties, which are from their crystalline counterparts. Among different bulk metallic glasses, Ti-based bulk metallic glasses are expected to be applied as biomedical materials due to high strength, high elastic limit, low Young's modulus, excellent corrosion resistance and good bioactivity of Ti element. Many Ti-based metallic glasses have been developed in Ti-Cu-Ni, Ti-Cu-Ni-Co, Ti-Cu-Ni-Zr, Ti-Cu-Ni-Zr-Sn, Ti-Cu-Ni-Sn-B-Si, Ti-Cu-Ni-Sn-Be, Ti-Cu-Ni-Zr-Be, Ti-Cu-Ni-Zr-Hf-Si and Ti-Cu-Ni-Zr-Nb (Ta) alloys, based on the Inoue's three empirical rules (Inoue, 1995) i.e., 1) multi-component consisting of more than three elements, 2) significant atomic size mismatches above 12% among the main three elements, and 3) negative heats of mixing among the main elements.

2. Problem description

Bulk metallic glasses have been extensively explored owing to their fundamental scientific importance and engineering applications. Bulk metallic glasses exhibit unique properties, e.g. high strength about 2-3 times of its crystalline counterparts, large elastic limit about 2% which is very near to some polymer materials, high corrosion resistance, high wear resistance, etc. These properties, which can be rarely found in crystalline materials, are attractive for the practical application as a new class of structural and functional materials. Although many Ti-based bulk metallic glasses have been developed during the past two decades, all the Ti-based bulk metallic glassy alloys with good glass-forming ability contain

some toxic elements of Ni and/or Be, which can cause an allergy, cancer or other diseases, limiting the application of Ti-based bulk metallic glasses in medical fields. Recently the Ti-based bulk metallic glasses without Ni were in Ti-Zr-Cu-Pd-Sn and Ti-Zr-Cu-Pd alloy systems in our group. Investigations on corrosion properties of the Ti-Zr-Cu-Pd-Sn bulk metallic glasses revealed that these glassy alloys are promising biomaterials due to their spontaneously passivated ability in simulated body fluid. And Ti-Zr-Cu-Pd alloy system shows a larger glass-forming ability with a critical diameter of 6 mm. Furthermore, higher strength and lower Young's modulus of 2000 MPa and 90 GPa have been obtained in Ti-Zr-Cu-Pd, which is much higher and lower than that of Ti-6Al-4V alloy. The development of new Ni-free Ti-Zr-Cu-Pd-Sn and Ti-Zr-Cu-Pd bulk metallic glasses exhibiting large glass-forming ability, high strength and distinct plastic strain fabricated make it possible that Ti-based bulk metallic glasses are applied as biomaterials. In this chapter, we will descript the relationship between corrosion properties, mechanical properties and microstructure as well as bioactivity of the Ni-free Ti-based bulk metallic glasses. Those properties are very important for metallic implants for application as artificial dental root materials or other biomedical materials. We succeeded in resolving the following problems which limit the application of Ti-based bulk metallic glasses in biomedical fields. First is that we developed the novel Ni-free Ti-based bulk metallic glasses since most of the Ti-based bulk metallic glasses with large glass-forming ability contain some toxic elements of Ni and/or Be, which will cause an allergy, cancer or other diseases in human body. The second one is that large plastic deformation was obtained in the Ti-based nano-crystalline/glassy composite alloys. The third one is that good bioactivity has been achieved in the new developed Ti-based bulk metallic glasses after some pre-treatments.

3. Experimental results

3.1 Mechanical property and microstructure

Bulk metallic glasses usually exhibit low plasticity due to the absence of dislocation activities and strain hardening. Therefore, for real applications, it seems important to improve the ductility of bulk metallic glasses without a significant sacrifice in the strength. To improve the plasticity of bulk metallic glasses, extensive research has been done over the past two decades. The low plasticity is caused by inhomogeneous plastic deformation, i.e., the severe shear localization. The general method is to introduce second phases in the metallic glassy matrix to inhibit the rapid propagation of shear bands. Furthermore, these second phases can interact with shear bands and effectively induce multiplication, branching, and restriction of shear bands to increase the plasticity of bulk metallic glasses. The second phases include nano-crystals (quasi-crystals), crystalline particles, fibers, ceramics and pores. To fabrication bulk metallic glassy composite, one common method is to change the composition or heat the as-cast bulk metallic glasses forming an in-situ second phases.

3.1.1 Thermal stability and microstructure

In order to improve the ductility of $Ti_{40}Zr_{10}Cu_{36}Pd_{14}$ bulk metallic glass, we take two approaches of heat treatment and changing the composition. Firstly we heat treated the as-cast $Ti_{40}Zr_{10}Cu_{36}Pd_{14}$ bulk metallic glass at different temperatures. The as-cast $Ti_{40}Zr_{10}Cu_{36}Pd_{14}$ bulk metallic glass shows a distinct glass transition temperature, $T_{g,}$ of 669 K, an onset temperature of crystallization, T_x, of 720 K, followed by two-stage

crystallization processes (Fig. 1). When the as-cast glassy alloy is isothermally annealed at 693 K (between T_g and T_x) for 10 min, partial crystallization occurs, corresponding to a crystallization fraction of about 20%. The fraction was evaluated by comparing the crystallization enthalpy of the exothermic peaks of the as-cast alloy with that of the annealed alloys. With increasing its annealing temperature to 723 K, the first crystallization peak disappears and its crystallization fraction reaches about 40 %. After annealing at 823 K for 10 min, the residual glassy phase is completely crystallized.

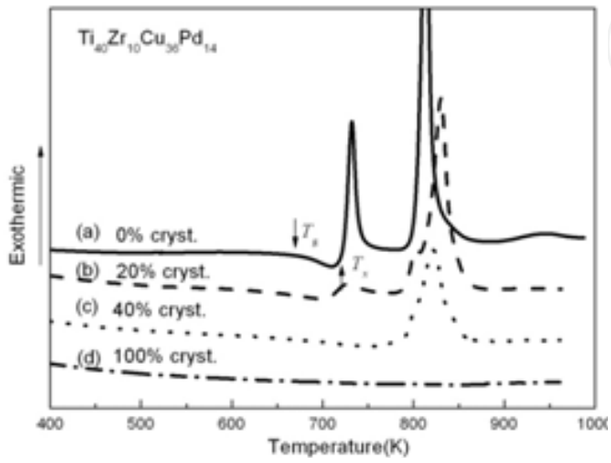

Fig. 1. DSC curves of the $Ti_{40}Zr_{10}Cu_{36}Pd_{14}$ bulk metallic glass and its annealed alloys: as-cast (a), annealed at 693 K (b), 723 K (c) and 823 K (d) for 10 min.

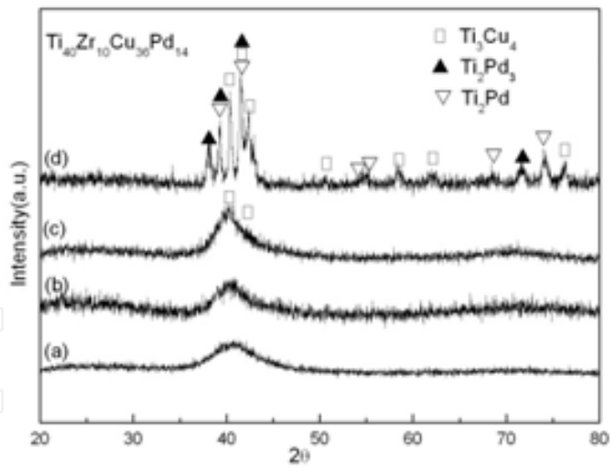

Fig. 2. XRD patterns of the $Ti_{40}Zr_{10}Cu_{36}Pd_{14}$ bulk metallic glass and its annealed alloys: as-cast (a), annealed at 693 K (b), 723 K (c) and 823 K (d) for 10 min.

Only a halo peak appears in the XRD pattern of the as-cast $Ti_{40}Zr_{10}Cu_{36}Pd_{14}$ bulk metallic glass, indicating that a glassy phase is formed in the cast alloy (Fig. 2). Although no obvious crystalline peaks appear in the XRD pattern after annealing at 693 K, the main halo peak becomes sharper as compared with the as-cast alloy, and some weak diffraction peaks identified as Ti_3Cu_4 appear in the pattern of the alloy annealed at 723 K. The low intensity peaks of the precipitates indicate the possibility of forming a nano-crystalline structure in

the glass matrix for the samples after annealing at 693 and 723 K, which can not be identified by XRD. Recently it was reported that (Jiang, 2003), in Cu–Zr–Ti bulk metallic glasses, significant volume fractions of nano-crystals embedding in the glassy matrix were observed in their HRTEM images, even if only one broad peak was found by XRD. On the other hand, the bulk metallic glass crystallized completely by annealing at 823 K. Many crystalline phase peaks appear and can be identified as tetragonal Ti_3Cu_4, orthorhombic Ti_2Pd_3 and tetragonal Ti_2Pd.

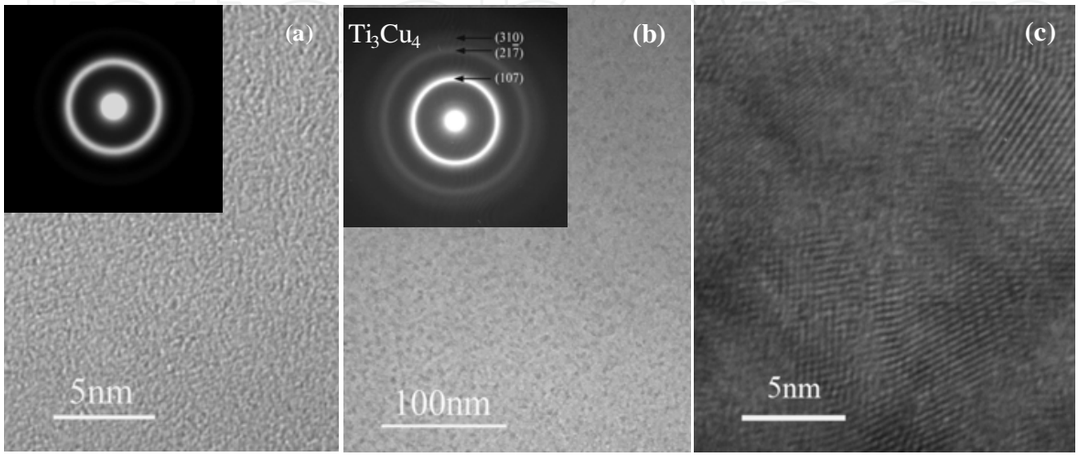

Fig. 3. HREM images, TEM images and corresponding selected area diffractions of the $Ti_{40}Zr_{10}Cu_{36}Pd_{14}$ as-cast bulk metallic glass (a) and alloy annealed at 693 K (b) and (c).

In microstructure, the as-cast bulk metallic glass has a typical glassy structure. Neither ordered structure nor crystalline phase is observed. Furthermore, only one halo ring appears in the corresponding SAED pattern. Figure 3 (b) and (c) show bright field TEM and HREM images of the alloy annealed at 693 K for 10 min. A mixed structure consisting of nano-particles homogeneously embedded in the glassy matrix is observed. The SADP consists of several ring patterns superimposed on a diffuse halo patterns, also indicating a mixture of nano-crystalline and residual glassy phase. The nano-particles are identified as a tetragonal

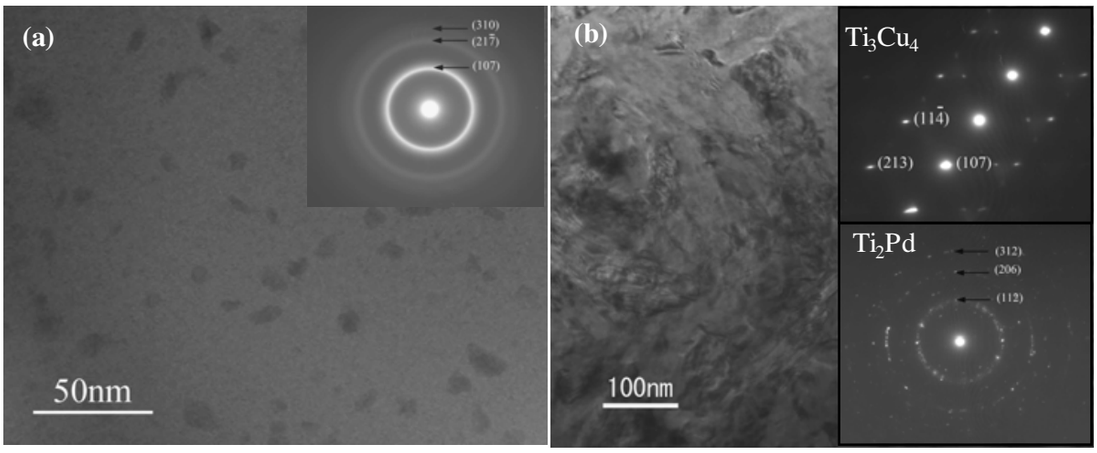

Fig. 4. Bright field TEM images and corresponding selected area diffractions of the $Ti_{40}Zr_{10}Cu_{36}Pd_{14}$ alloys annealed at 723 K (a) and 823 K (b).

Ti_3Cu_4. The HREM image of the same specimen in Fig. 3 (c), shows that the size of nano-Ti_3Cu_4 is less than 5 nm. The results are consistent with that of XRD in Fig. 2. By annealing at 723 K, Ti_3Cu_4 nano-particles grow up accompanying with the increase in the diffraction intensity of (107), $(21\bar{7})$ and (310) crystal planes (Fig. 4 (a)). With annealing temperature to 823 K, a Ti_2Pd was also identified in addition to Ti_3Cu_4 phase (Fig. 4 (b)).

3.1.2 Mechanical properties and fracture morphology.

The deformation of the as-cast bulk metallic glasses occurs mainly by elastic deformation (Fig. 5). The fracture surface shows a typical vein pattern originating from the deformation of narrow shear band. The partly nano-crystallized alloy annealed at 693 K exhibits high strength of 2165 MPa (Fig. 5 (b)), which is higher than those of the as-cast alloy and other annealed alloys. Furthermore, distinct plastic deformation of about 0.8 % for the partly nano-crystallized alloy after annealing at 693 K is also observed presumably because the nano-particles can suppress the deformation of shear bands and a high density of free volumes can be introduced by the annealing treatment in the supercooled liquid region. In addition, the fracture surface of the alloy annealed at 693 K is still in the vein-like pattern

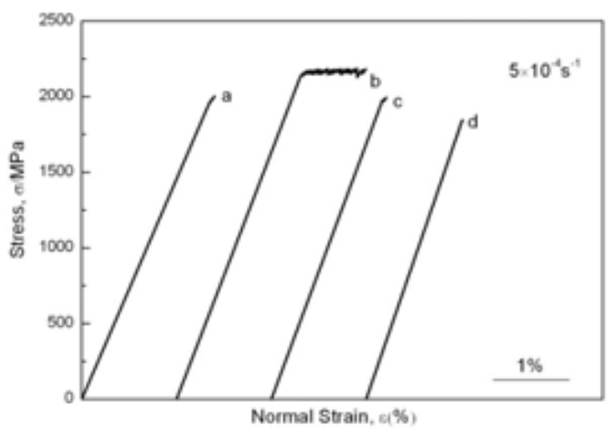

Fig. 5. Compressive strain-stress curves of the $Ti_{40}Zr_{10}Cu_{36}Pd_{14}$ bulk metallic glass and its annealed alloys: as-cast (a), annealed at 693 K (b), 723 K (c) and 823 K (d) for 10 min

type (Fig. 6 (b)). With further increasing annealing temperature to 723 K, the fracture mode changes to a brittle type, shown in Fig. 6 (c) and (d). Xing et al. (Xing et al., 1998) found that the crystalline fraction of 40%-45% leads to the change in the fracture surface from ductile to brittle type and porosity plays an important role in multiple cracking of annealed alloys. Meanwhile, for the alloy annealed at 823 K, the fracture surface is a totally brittle fracture type as shown in Fig. 6 (e). At the same time, compressive strength decreased for the alloys annealed at 723 K and 823 K.

As above-mentioned, nano-crystalline structure is formed in the Ti-Zr-Cu-Pd bulk metallic glass subjected to an optimum annealing treatments. The crystallized structure changes seriously the mechanical properties and fracture morphology. That is, the deformation behavior is associated with the nature of crystallites precipitated in the glassy matrix. Annealing of the bulk metallic glass at 693 K for 10 min, i.e., between glass transition temperature and onset temperature of crystallization, results in the formation of nano-particles of Ti_3Cu_4 with sizes smaller that 5 nm in the glassy matrix.

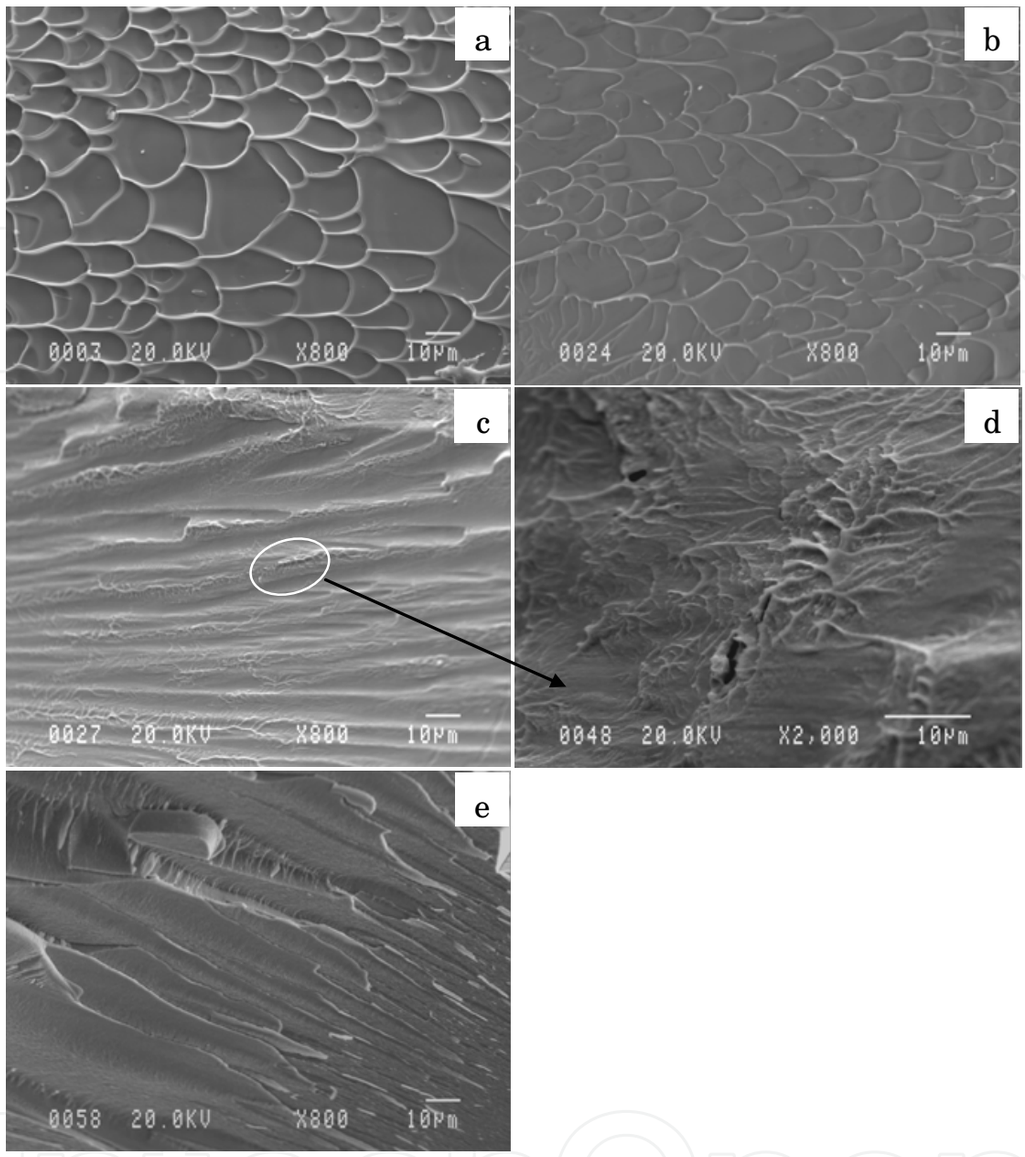

Fig. 6. Fracture morphologies of the $Ti_{40}Zr_{10}Cu_{36}Pd_{14}$ bulk metallic glass and its annealed alloys: as-cast (a), annealed at 693K (b), 723 K (c) (d), and 823 K (e) for 10 min.

In general, the formation of the nano-composite in metallic glass requires both the ease of homogeneous nucleation of crystalline phase and difficulty of the subsequent crystal growth. When the nano-particles are much smaller than the shear bands and the nano-particles are separated by glassy matrix (Xing et al., 1998), the deformation of the shear band is dominated by the glassy matrix, and the nano-particles will inhibit the deformation of the shear bands. Inoue et al. (Inoue, et al., 2000) classified the mechanism for high strength and good ductility of the bulk nano-crystalline alloys into two types by the nano-particles and remaining glassy matrix. The nano-particles with perfect crystal structure may act as inhibitor against shear deformation of the glassy matrix. In addition, the nano-particle/glassy matrix interface has a highly dense packed atomic configuration due to low interface energy. Furthermore, the localized deformation mode of the glassy matrix

enhances the deformability owing to the softening caused by the increase of temperature in the localized region. Then higher strength and good plastic deformation were obtained for the alloy annealed at 693 K. On the other hand, both the as-cast bulk metallic glass and the alloy annealed at 693 K show vein like patterns. There are several hypotheses those expatiate the vein pattern in fracture surface of the metallic glasses. One is proposed that the behavior of the shear band was similar to a thin viscous layer between two parallel plates under tension. During the process of deformation, shallow cavities originate and the bridges between them break, resulting in the veins. The other hypotheses mentioned the decrease of viscosity due to the intensive increase of the free volume in the shear band owing to a high hydrostatic tension. It is also found that local melting occurs within the shear band and melting droplets on the fracture surfaces of hydrostatic deformed glass result in vein like patterns. In this study, further annealing at 723 K for 10 min, i.e., the first crystallization peak, results in the growth of Ti_3Cu_4 phase and the increase of crystallization fraction. The deformation is not dominated by the glassy matrix when the nano-particles occupy a high volume fraction of 40 %. Consequently the brittle morphology was found in the alloy annealed at 723 K shown in Fig. 6 (c) and (d). Figure 6 (d) is the enlarged area of the circle area in Fig. 6 (c). Some pores are observed in the surface of the alloy annealed at 723 K, which act as crack initiators, and the alloy fails in a brittle manner (Dasa et al., 2005). It should be pointed out that the highest strength of 2100 MPa obtained in the $Ti_{40}Zr_{10}Cu_{36}Pd_{14}$ bulk nano-composite is much higher than that of Ti-6Al-4V alloy (Lűtjering et al., 1999).
High strength and distinct plastic strain have been also observed in the stress-strain curves for the Nb-added alloys (Fig. 7). Especially, yield strength exceeding 2050 MPa, low Young's modulus of about 80 GPa and distinct plastic strain of 6.5 % and 8.5 % corresponding to serrated flow sections are attributed to the propagation of narrow shear bands.

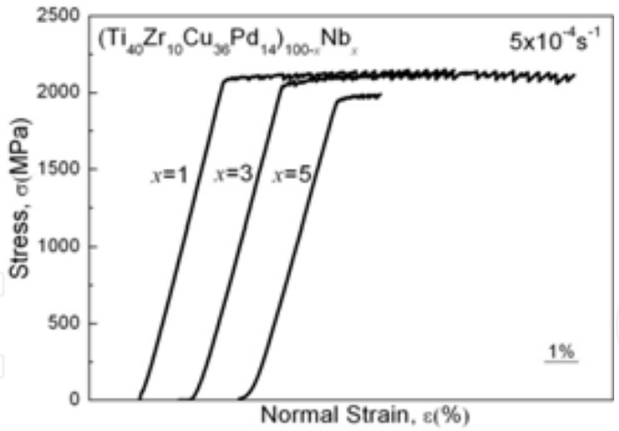

Fig. 7. Compressive strain-stress curves of the $(Ti_{40}Zr_{10}Cu_{36}Pd_{14})_{100-x}Nb_x$ as-cast rods with a diameter of 2 mm.

The fracture surface shows a vein pattern originating from the deformation of narrow shear band. With further increasing the content of Nb to 5 %, the plastic strain decreases to 1.0 %, not as large as the former ones. On the side surface, a number of shear bands are observed near the fracture edge of the 1 % and 3 % Nb-added alloys, and some of shear bands are jagged and interdicted, as shown in Fig. 8 (a) and (b).

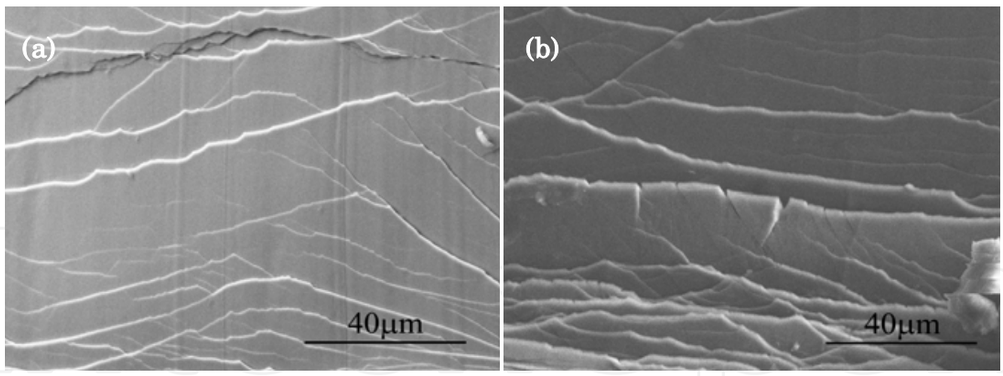

Fig. 8. Lateral surface of the $(Ti_{40}Zr_{10}Cu_{36}Pd_{14})_{100-x}Nb_x$ as-cast rods after fracture (a) x=1, (b) x=3.

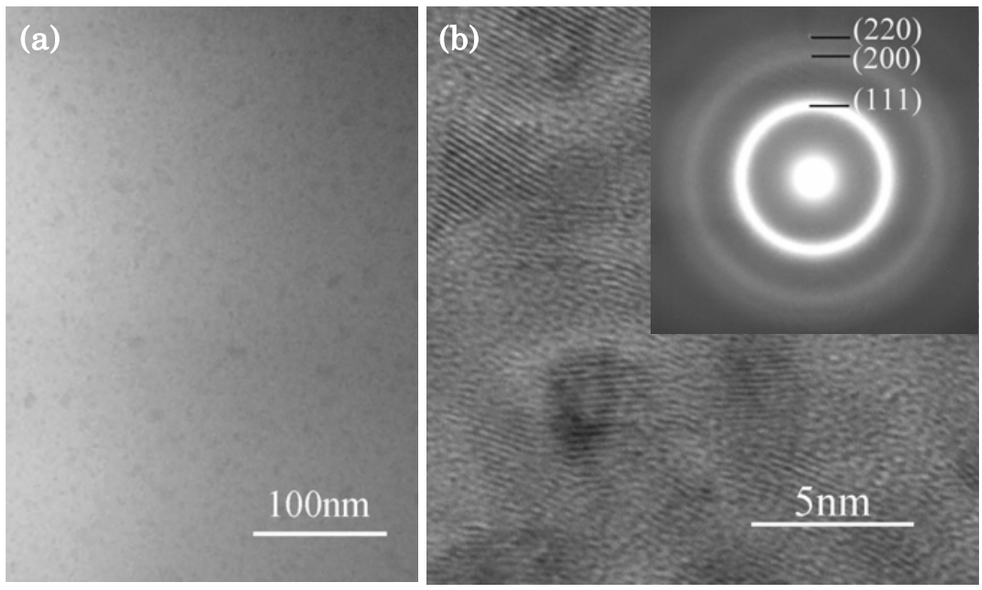

Fig. 9. Bright-field TEM (a) and HREM (b) images as well as corresponding SAD pattern of the $(Ti_{40}Zr_{10}Cu_{36}Pd_{14})_{100-x}Nb_x$ as-cast rods, x=1.

Some nano-particles with volume fraction of 8 % are uniformly dispersed the glassy matrix for 1 % Nb-added rod (Fig. 9 (a) and (b)). The HREM image of the 1 % Nb-added rod shows that the size of nano-particles is smaller than 5 nm in Fig. 9 (b). Several ring patterns superimposing on the diffuse halo ring in corresponding SAD pattern also indicates a mixture of nano-crystalline and residual glassy matrix. The nano-particles are identified as a Pd_3Ti phase with crystal planes of (111), (200) and (220). With 3 % Nb addition, the ring patterns superimposed on the diffuse halo ring in SAD pattern are sharper because of the increase in the volume fraction of Pd_3Ti nano-particle to 13 % (Fig. 10). With further increasing Nb content to 5 %, the volume fraction of nano-particles increases to 20 % associated with the increase of their size as shown in Fig. 11. The NBD pattern taken from the nano-particle along its [111] zone axis confirms the cubic structure as the Pd_3Ti with the lattice parameter a=0.3167nm. The particle size of Pd_3Ti phase increases accompanying with the increase in the diffraction intensity of (111), (200), (220) and (311) crystal planes. The TEM results showing obvious nano-particles with several nano-meters are not contradicted with the amorphous-like peak in XRD patterns.

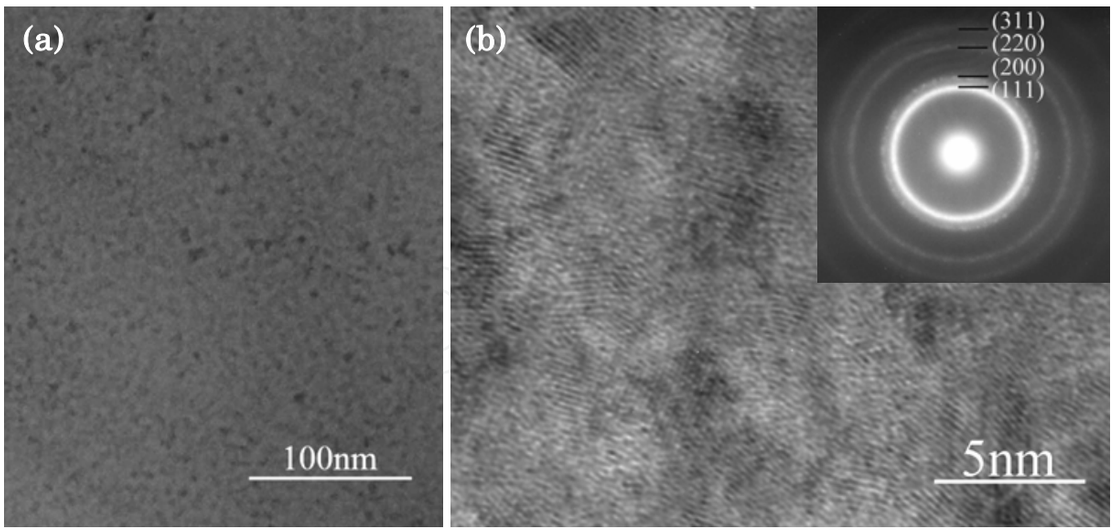

Fig. 10. Bright-field TEM(a) and HREM(b) images as well as corresponding SAD pattern of the $(Ti_{40}Zr_{10}Cu_{36}Pd_{14})_{100-x}Nb_x$ as-cast rod, x=3.

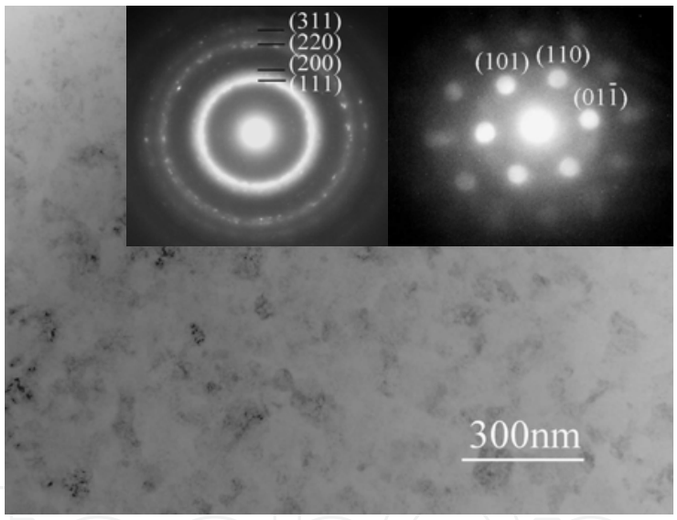

Fig. 11. Bright-filed image and corresponding SAD pattern as well as NBD pattern of the $(Ti_{40}Zr_{10}Cu_{36}Pd_{14})_{100-x}Nb_x$ as-cast rod, x=5.

Good mechanical properties of Ti-Zr-Cu-Pd-Nb bulk metallic glass are also attributed to the mixed state of nano-particles and glassy matrix. The size and volume fraction of Pd_3Ti nano-particles in the Ti-Zr-Cu-Pd-Nb bulk metallic glass can be distinctly changed with different Nb additions. Consequently, it is conduced that the microstructure consisting of nano-particles and glassy phase improves significantly the mechanical property of Ti-Zr-Cu-Pd-Nb alloys.

3.2 Corrosion behaviour

The potentiodynamic polarization curves of the Ti-based bulk metallic glass and its crystalline alloys in Hanks' solution at 310 K are shown in Fig. 12. For the sake of comparison the data of a commercial Ti-6Al-4V alloy were also included in the figure. In

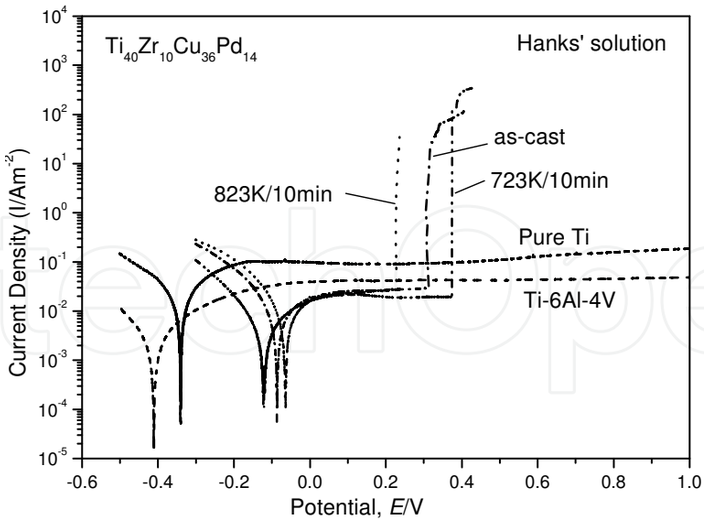

Fig. 12. Anodic and cathodic polarization curves of the $Ti_{40}Zr_{10}Cu_{36}Pd_{14}$ bulk metallic glass and its crystalline alloys at 310 K in Hanks' solution.

Hanks' solution, both the as-cast bulk metallic glass and its crystalline counterparts are spontaneously passivated. With further increase anodic potential, the passivity breakdown occurs. It is seen that the passive current densities and pitting potentials in Hanks' solution are dependent on the annealing temperatures. The as-cast bulk metallic glass and the alloy after annealing below 723 K have lower passive current densities located about 10^{-2} A/m^2, lower than that of commercial Ti-6Al-4V alloy, meaning that more protective and denser passive film formed on the surface of the alloys in the anodic process. Furthermore, noble pitting potential has been observed for the partly crystalline alloy annealed at 723 K. The pitting potentials for the as-cast glass and the alloys annealed below 723 K are about several hundreds of microvolts higher than their open-circuit potentials, meaning that spontaneous pitting corrosion may not occur in human body environment. However, the fully crystalline alloy annealed at 823 K exhibits a much higher passive current density and a lower pitting potential.

In AES depth profiles of the as-cast $Ti_{40}Zr_{10}Cu_{36}Pd_{14}$ bulk metallic glass and its crystalline alloys after immersion in Hanks' solution at 310 K for 168 h (Fig. 13). The thickness of the oxide layer was estimated from the thickness where the oxygen concentration became 50%. The concentration of each metal element comes from both oxidic state and metallic state because difference in chemical states could not be distinguished by AES. It is obvious that the oxide films formed on all the alloys are smaller than 5 nm, suggesting high corrosion resistance of the alloy system. The surface films formed on the as-cast and crystalline alloys in Hanks' solution mainly contain titanium, especially in their outermost region. In addition, the concentration of Zr is also higher that of nominal concentration in the bulk. The comparison of the thickness of the oxide film reveals that the layers formed in Hanks' solution for the as-cast metallic glass and the nano-crystalline alloy annealed at 723 K are thinner than that of the completely crystalline alloy annealed at 823 K. The thicker film formed on the completely crystalline sample in Hanks' solution is due to a higher oxidation rate of the fully crystalline alloy. Recently it has been reported that partial nano-crystallization of the glassy alloys exhibited higher corrosion resistance in Cr-based,

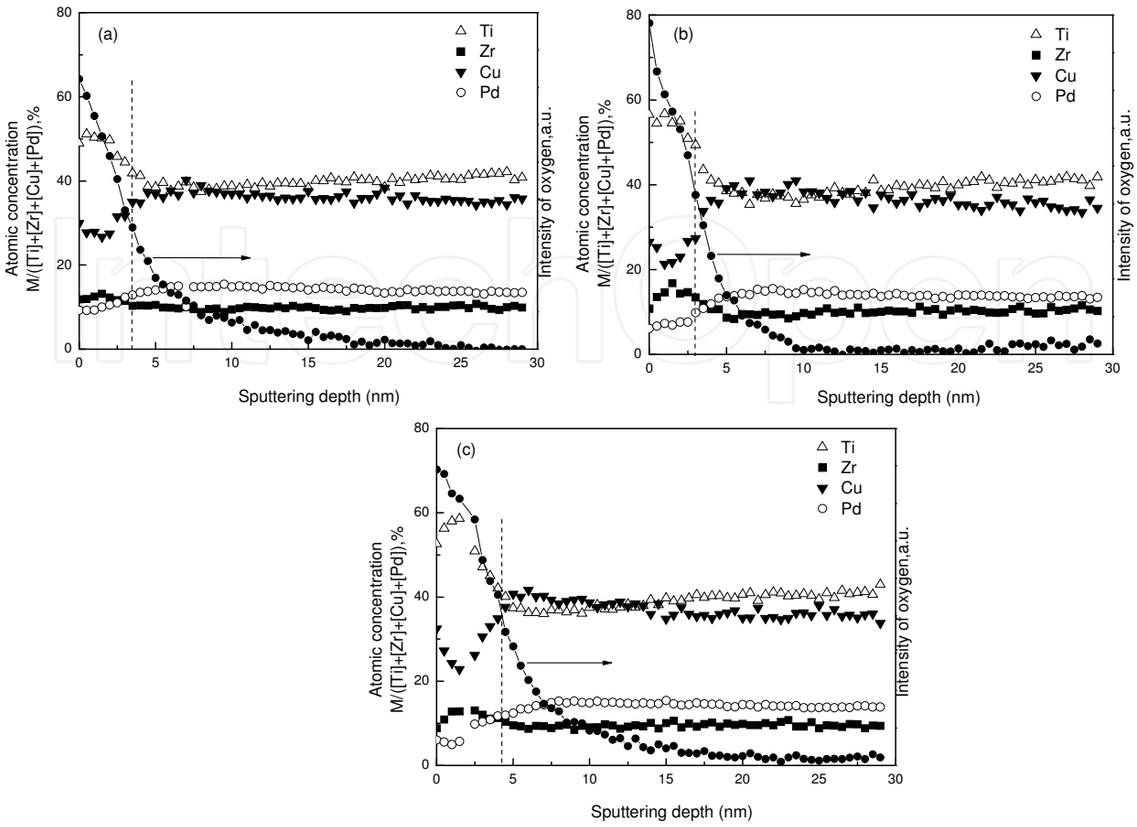

Fig. 13. AES depth profiles of the $Ti_{40}Zr_{10}Cu_{36}Pd_{14}$ bulk metallic glass and its crystalline alloys after immersion at 310 K in Hanks' solution for 168 h as-cast (a) and annealed at 723 k (b) 823 K (c).

Ni-based, Zr-based and Fe-based glassy alloys. Some authors (Mondal et al., 2005) attributed higher corrosion resistance to the structure relaxation and stress relief caused by annealing. That is because structural relaxation decreases the free energy of the alloy, consequently decreases the elemental reactivity and increases the alloy's chemical stability. Some authors (Mehmood et al., 1998, Alvarez et al., 1998) considered that the formation of nano-particles induced more protective films formed in the underlying surface. The Zr-rich nano-crystalline phases formed after heat treatment in Cr-Zr alloys ennobled the pitting potential in aggressive HCl solution due to the fact that the formation of the hcp zirconium phase leads to an increase in the Cr content of the matrix phase which is able to form thin protective Cr-rich passive films covering the entire homogeneous alloy surface. But the pitting potential of the Cr-Zr alloys after heat treatment was also dependent on the heating temperature, i.e. the size of nano-crystalline phase played an important role. When the size of nano-crystalline phases exceeds a critical size of 20 nm, the protective passive films can't completely cover the precipitates and the pitting corrosion reduced. In this study, enhancement of pitting potential of partly nano-crystalline alloy annealed at 723 K as shown in Fig. 5, can be explained by the formation of Ti_3Cu_4 phase, resulting in the enrichment of Pd in the glassy matrix, which is helpful to form protective passive film. At the same time, the phases are in the nano-scale, thus a large number of interface defects are expected in the nano-crystalline alloys. The breakdown of passive film is more uniform because of more

defects in the passive film, leading to uniform corrosion. More uniform distribution of the passive current density over the preferred corrosion attack sites allows the nano-crystalline alloys to maintain passivity over large potential range on the noble side and resist localized Cl ion attack (Mehmood et al., 1998). Whereas $Ti_{40}Zr_{10}Cu_{36}Pd_{14}$ bulk metallic glass is completely crystallized, not only Ti_3Cu_4 phase but also Ti_2Pd and Ti_2Pd_3 nucleate and grow-up to larger size, it may cause micro-galvanic corrosion between Cu-rich phase and Pd-rich phases. Thus higher passive current density is observed, indicating that both the size and composition of crystalline phase play an important role in controlling the corrosion behavior of Ti-based alloys.

3.3 Bioactive property

A simple chemical and thermal two-step treatment method has been widely used because the bone-like apatite can be formed on conventional alloys in biomimetic solutions. However this method seems to be ineffective on Ti-based bulk metallic glasses. In this study, a new two-step method consisting of hydrothermal-electrochemical treatment followed by pre-calcification treatment is developed. The nucleation and growth of bone-like apatite on the $Ti_{40}Zr_{10}Cu_{36}Pd_{14}$ metallic glass are investigated.

A microporous and network structure is formed on the surface of $Ti_{40}Zr_{10}Cu_{36}Pd_{14}$ metallic glass after treatment in 1 M NaOH solution at 90 °C for 2 h under a direct current density of 2 mA/cm², as shown in Fig. 14(a). A grown composite layer with the whole thickness of about 500 nm is observed in the cross section of the treated $Ti_{40}Zr_{10}Cu_{36}Pd_{14}$ metallic glass. The outer layer is the porous and network layer formed by the reaction of the alloy components with the alkali solution under the above mentioned experimental condition. The inner layer is the intermediated layer lying between the metallic glass substrate and the outer porous layer, which is formed by elemental diffusion to the outer layer. In addition, Cu and Pd elements are detected by EDS on the surface of the counter electrode Pt. These elements are dissolved from the metallic glass anodic electrode and deposit on the counter electrode Pt.

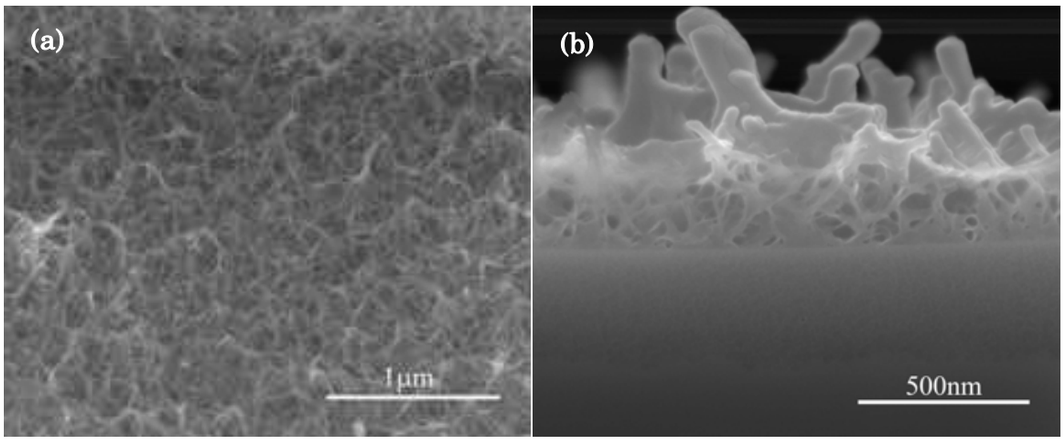

Fig. 14. SEM surface morphology (a) and cross section morphology (b) of $Ti_{40}Zr_{10}Cu_{36}Pd_{14}$ metallic glass after electrochemical-hydrothermal treatment in 1 M NaOH solution.

Some white nuclei distributed on the surface of the electrochemical-hydrothermal treated $Ti_{40}Zr_{10}Cu_{36}Pd_{14}$ metallic glass subjected to pre-calcification treatment (Fig. 15). The sizes of

nuclei are about 1 μm in length and enriched with Ca and P elements analyzed by EDS (Fig. 15 (b)). Under high magnification, some smaller white granules can also be observed. Both HPO_4^{2-} and Ca^{2+} ions could be adsorbed into the micro-porous titanium oxide surface to stimulate the nucleation and growth of dicalcium phosphate during immersion in Hanks' solution.

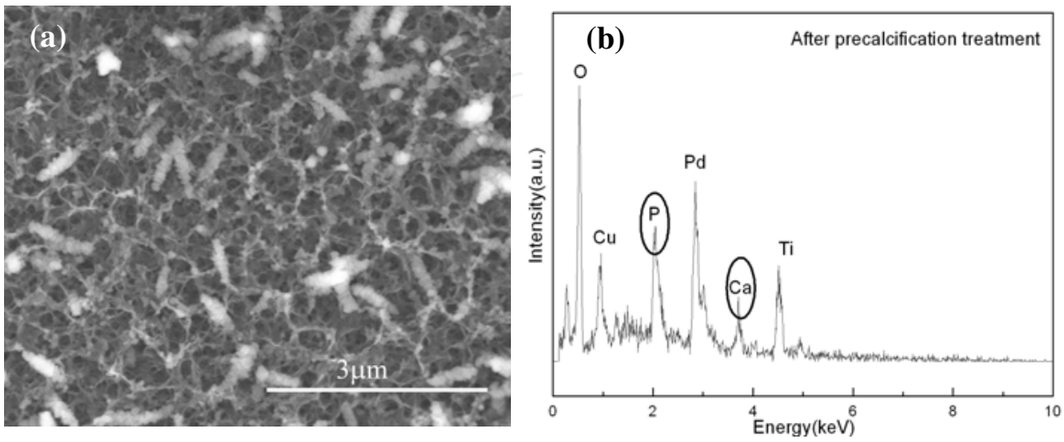

Fig. 15. SEM image (a) and EDS spectrum (b) of electrochemical-hydrothermal treated $Ti_{40}Zr_{10}Cu_{36}Pd_{14}$ metallic glass after pre-calcification treatment.

After soaking in Hanks' solution for one day, a thin and homogeneous layer appears in the network surface (Fig. 16 (a)), which is composed of Ca, O and P. The Ca/P ratio is identified to be 1.3 by EDS. Then the layer grows and the Ca content increases with an increase of immersion time. With further increasing time to six days, the Ca/P ratio reaches about 1.6, which is similar to the ratio of apatite. From the cross section SEM image of the two-step treated $Ti_{40}Zr_{10}Cu_{36}Pd_{14}$ metallic glass after immersion in Hanks' solution for six days shown in Fig. 17, it is obvious that the porous apatite is strongly bonded with the porous surface of the metallic glass in the absence of a visible interface after the electrochemical-hydrothermal treatment. The thickness of the resulting apatite probable is about several hundreds nanometers. However, if the samples were only performed by hydrothermal treatment with pre-calcification or by hydrothermal-electrochemical treatment without pre-calcification, no calcium phosphate precipitation was observed on the surface of $Ti_{40}Zr_{10}Cu_{36}Pd_{14}$ metallic glass even after immersion in Hanks' solution for 30 days.

In the XRD pattern of the surface of the $Ti_{40}Zr_{10}Cu_{36}Pd_{14}$ metallic glass after immersion in Hanks' solution for 4 days, as shown in Fig. 18. The peaks arising from apatite as well as a broad peak at about 46.5° from the metallic glass substrate are identified. It indicates that the substrate remains a glassy state after the treatment. The hydrothermal-electrochemical pretreatment temperature of 90 °C is much lower than the glass transition temperature (396 °C) of $Ti_{40}Zr_{10}Cu_{36}Pd_{14}$ bulk metallic glasses. Therefore, after such a serious treatment, the substrate remains a glassy state as evident from XRD pattern, which is very important for retaining excellent properties of bulk metallic glasses in real application.

Figure 19 shows the AES spectra before and after sputtering to a depth of 1 μm as well as elemental depth profile of the hydrothermal-electrochemical treated $Ti_{40}Zr_{10}Cu_{36}Pd_{14}$ metallic glass. Strong Ti and O signals are detected on the surface together with small signal of Cu and C before sputtering. The depth profile shows that titanium oxide exists as a main phase on the

surface of the Ti-based metallic glass after subjected to hydrothermal- electrochemical method in alkali solution. After sputtering, all of Ti, Cu, Pd and Zr in the alloy can be detected.

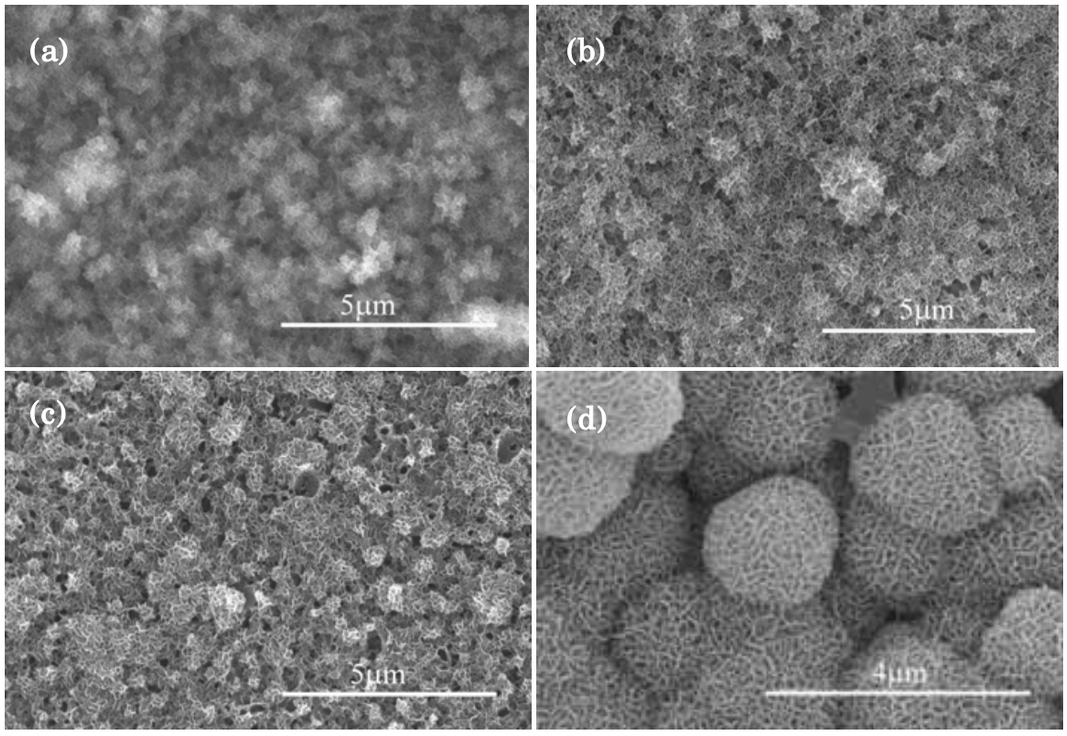

Fig. 16. SEM images of two-step pretreated $Ti_{40}Zr_{10}Cu_{36}Pd_{14}$ metallic glass after immersion in Hanks' solution for (a) one (b) two (c) three and (d) six days.

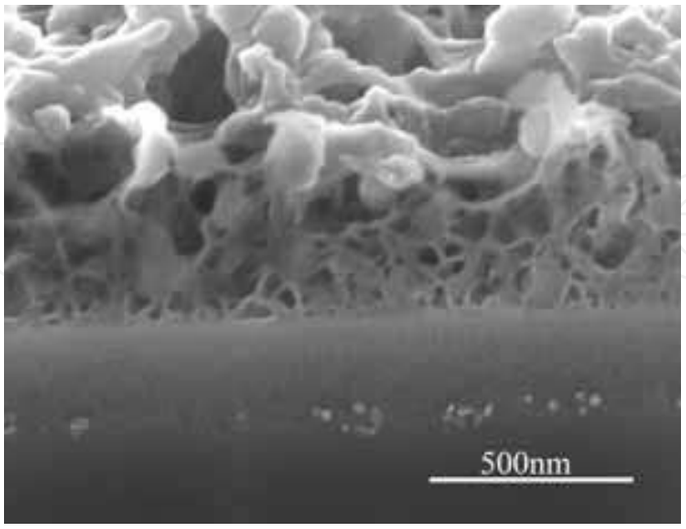

Fig. 17. Cross sectional SEM image of two-step treated $Ti_{40}Zr_{10}Cu_{36}Pd_{14}$ metallic glass after immersion in Hanks' solution for six days.

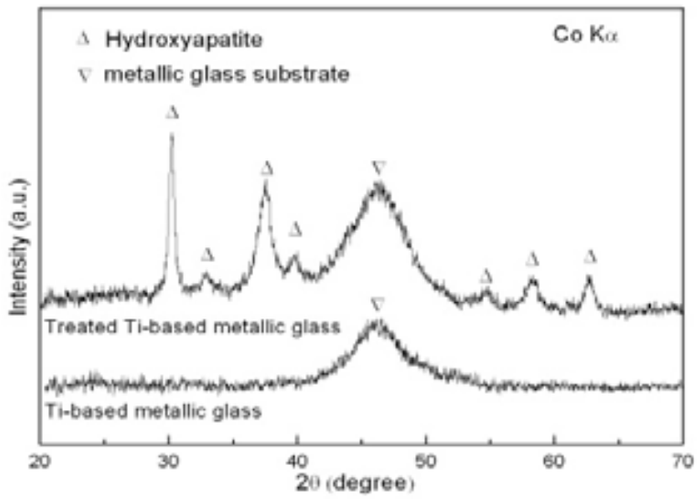

Fig. 18. XRD patterns of two-step treated the $Ti_{40}Zr_{10}Cu_{36}Pd_{14}$ metallic glass and monolithic $Ti_{40}Zr_{10}Cu_{36}Pd_{14}$ metallic glass after immersion in Hanks' solution for six days.

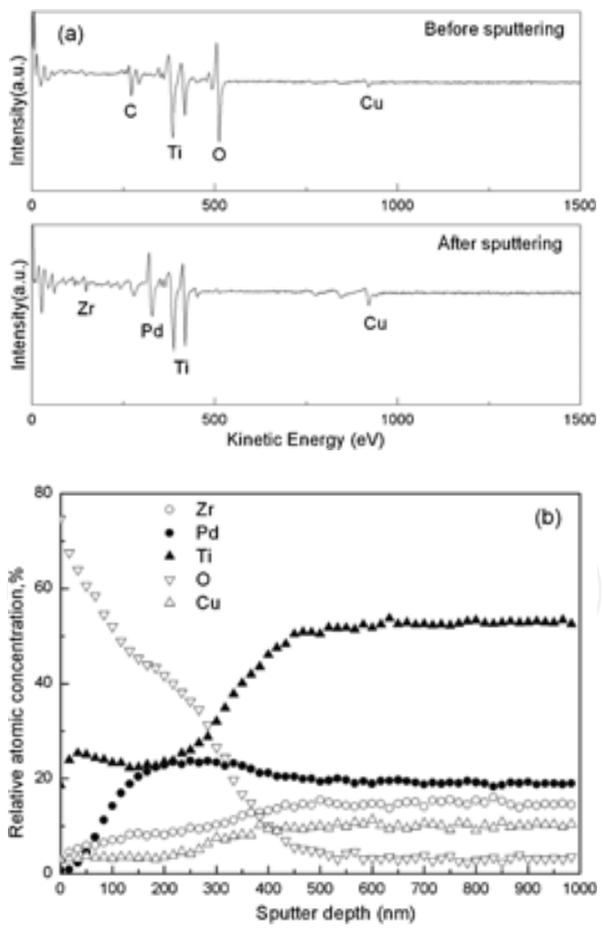

Fig. 19. AES spectra and elemental depth profiles of the electrochemical hydrothermal treated $Ti_{40}Zr_{10}Cu_{36}Pd_{14}$ metallic glass in 1 M NaOH solution.

The surface consists mainly of Ca, P and O before sputtering after immersion in Hanks' solution for six days (Fig. 20). It was also demonstrated that the Ca concentration increases with increasing immersion time in Hanks' solution. The above mentioned results indicate that only the combination of hydrothermal-electrochemical treatment and pre-calcification treatment causes the nucleation and improve growth rate of apatite on the $Ti_{40}Zr_{10}Cu_{36}Pd_{14}$ metallic glass. The bioactivity of metallic implants can be evaluated by the formation of apatite in body fluid and the growth rate of the apatite layer. Usually the possible mechanism of nucleation and growth of apatite on alkali pretreated alloy immersion in SBF has been proposed as follows (Shukla et al., 2006): 1) A sodium titanate gel layer is formed on the surface after alkali treatment; 2) Na^+ ion releases into the surrounding SBF via an ion exchanging with H_3O^+ to form Ti-OH group; 3) The Ti-OH groups interact with Ca to form a calcium titanate; 4) The calcium titanate reacts with phosphate ion to form apatite nuclei; 5) Once the nuclei are formed, the apatite nuclei automatically grow up by consuming the Ca and P ion in surrounding fluid. According to the above idea, sodium titanate hydrogel film formed after alkali treatment can initiate apatite nucleation itself.

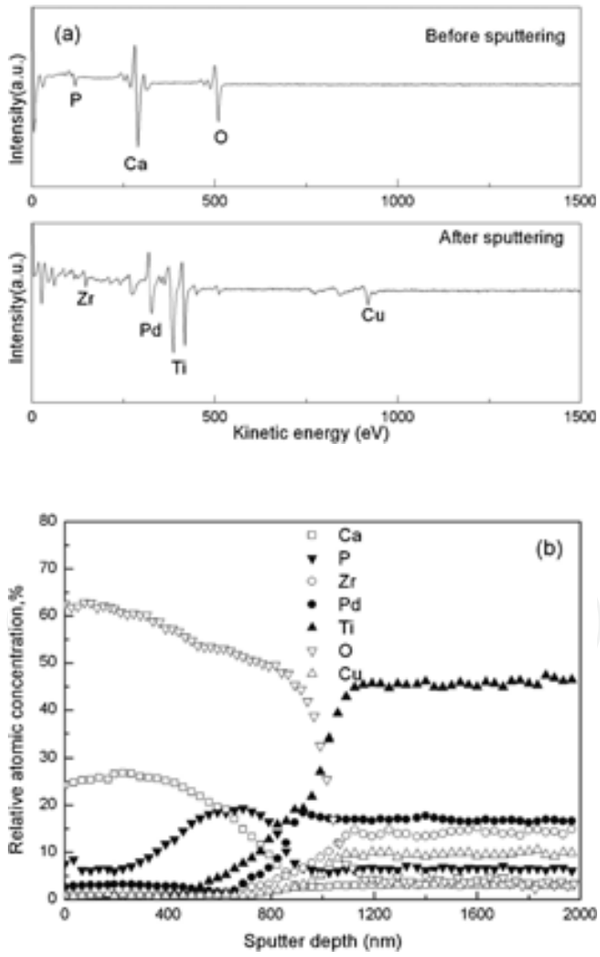

Fig. 20. AES spectra and elemental depth profiles of the two-step treated $Ti_{40}Zr_{10}Cu_{36}Pd_{14}$ metallic glass after immersion in Hanks' solution for six days.

Our previous work revealed that simple alkali soaking at 60 °C even for one day, can't induce the formation of apatite on the surface of Ti-based bulk metallic glasses due to high concentration other metals such as Cu, Pd and Zr. The effect of the hydrothermal-electrochemical treatment can increase the surface roughness as well as the Ti concentration on the outer layer of metallic glass. In addition to the hydrothermal-electrochemical treatment in 1 M NaOH solution, a much thicker TiO_2 layer, instead of native thin TiO_2 layer, is formed, which is beneficial to the nucleation of apatite. Thus, the hydrothermal-electrochemical treatment is effective of high surface roughness and negative-charged TiO_2 layer of metallic glass.

After hydrothermal-electrochemical and hydrothermal treatments in NaOH, an amorphous sodium titanate gel layer is formed as shown in formula (1). Sodium ions are released from the surface via NaOH dissolving in water when the samples are completely washed by distilled water as formula (2).

$$TiO_2 + NaOH \rightarrow NaHTiO_3 \tag{1}$$

$$NaHTiO_3 + H_2O \rightarrow TiO_2 \cdot OH^- + H^+ + NaOH \tag{2}$$

Therefore, no sodium can be observed by EDS or AES after hydrothermal treatment. Our results indicate that the exchanging process between Na^+ ion and H_3O^+ which initiates the apatite nucleation don't have to occur in SBF. It is suggested that the micro-porous surface leads to the adsorption of Ca and P ions. The spatially submicron-scaled micro-architecture of the treated samples was one of the most probable factors. It is well known that the surface modification of Ti alloys is necessary in order to improve implant-tissue osseo-integration. In particular, TiO_2 layer on the surface of Ti alloys plays an important role in determining biocompatibility and corrosion behavior of Ti implant alloys. Furthermore, the hydrothermal-electrochemical treatment at low temperature is suitable for a metallic glassy alloy which will be crystallized by annealing at high temperature around glass transition temperature.

On the other hand, only the hydrothermal-electrochemical treatment, failed to form an active surface on the Ti-based metallic glass. The pre-calcification procedure accelerated the calcium phosphate precipitation on the surface of electrochemical-hydrothermal treated $Ti_{40}Zr_{10}Cu_{36}Pd_{14}$ metallic glass. As mentioned in the results, calcium phosphate can't precipitate on the surface of the hydrothermal-electrochemical treated metallic glass without pre-calcification treatment soaking in Hanks' solution even for 30 days. The pre-calcification treatment is necessary to acquire the nuclei of Ca-P inducing the growth of bone-like apatite. Ca-P coating can also be inducted on titanium surface with treatment of H_3PO_4 pretreatment (Feng et al., 2002), $Ca(OH)_2$ pretreatment (Yang et al, 2006) or combination treatment of Na_2HPO_4 and $Ca(OH)_2$ treatments. All the above pretreatment can accelerate the nucleation of calcium phosphate on Ti. In addition, this calcium phosphate nucleates homogeneously and grows up to layer upon layer. Before the samples were immersed in Hanks' solution, HPO_4^{2-} and Ca^{2+} ions were adsorbed homogeneously onto the micro-porous and network surface on $Ti_{40}Zr_{10}Cu_{36}Pd_{14}$ metallic glass. The hydrothermal-electrochemical treatment makes a much larger surface area on the Ti metallic glass than that without current two-step treatments. The micro-porous surface leads to much more adsorption of HPO_4^{2-} or/and Ca^{2+} ions stimulating the nucleation of calcium phosphate layer on Ti-based metallic glass

followed by immersion in Hanks' solution (Healy, 1992). From the AES in Fig. 20, the consuming process of Ca ion can be found. Then a homogeneous calcification phosphate layer formed on the surface, rather than an island nucleate.

As mentioned in a previous work, the $Ti_{40}Zr_{10}Cu_{36}Pd_{14}$ bulk metallic glass can be fabricated in the diameter range up to 6 mm. In this research, $Ti_{40}Zr_{10}Cu_{36}Pd_{14}$ ribbon samples were used for convenience. There must be no problem to achieve the same results in the bulk samples with the same alloy composition. The present hydrothermal-electrochemical and pre-calcification treatments seem to be more suitable for the application of the Ti-based bulk metallic glasses, owning to a relative low concentration of Ti. This study demonstrates that the combination of hydrothermal-electrochemical treatment and pre-calcification treatment can dramatically accelerate the nucleation and growth of calcium phosphate on the surface of Ti-based metallic glass. For conventional Ti-6Al-4V, Ti-Zr-Nb or other alloys, it may be also a promising method. We may propose the formation mechanism of apatite on Ti-based metallic glass as follows. Step one of hydrothermal-electrochemical treatment might have three effects on the as-prepared metallic glass surface. The first is an increasing concentration of Ti on the outer surface by forming a porous layer. The second is the formation of micro-porous network structure in the aggressive boiling alkali solution. The third is the formation of thicker titanium oxide layer in the outer surface than that of native titanium oxide layer. Ti-OH groups are also presented on the porous TiO_2 surface. Negative-charged and micro-porous surfaces are the main reason for the good bioactivity (Heuer et al., 1992). Step two of pre-calcification treatment stimulates the adsorption of HPO_4^{2-} and Ca^{2+}, which are necessary for the nucleation of apatite. Once formed, bone-like apatite grows up by consuming calcium and phosphate ions in surrounding simulated body fluid. The apatite is strongly bonded with the similar porous structure on the surface of the electrochemical-hydrothermal treated $Ti_{40}Zr_{10}Cu_{36}Pd_{14}$ metallic glass without a visible interface.

4. Conclusion

In this chapter, we research on mechanical property, corrosion behavior, microstructure and bioactivity of Ni-free Ti-Zr-Cu-Pd (-Nb) bulk metallic glasses or its crystallized counterpart alloys. The results were concluded as follows,

The strength and plastic deformation can be improved by compositing bulk metallic glasses with nano-crystals produced by heat treatment or in-situ casting by changing of composition. Nano-composites are formed in the alloys annealed at 693 and 723 K. High strength of over 2100 MPa and distinct plastic deformation of 0. 8% are obtained in the alloy annealed at 693 K. The minor addition of Nb to Ti-Zr-Cu-Pd bulk metallic glasses induced the formation of Pd_3Ti nano-particles by copper mold casting. High yield strength of over 2050 MPa, low Young's modulus of about 80 GPa and distinct plastic strain of over 6.5 % were achieved in 1 % and 3 % Nb-added alloys, due to the nano-particles dispersed in the glassy matrix blocks the propagation of shear bands. With further increasing Nb content to 5 %, the plastic strain decreased to 1.0 %. The most optimum Nb addition was 3 %.

The $Ti_{40}Zr_{10}Cu_{36}Pd_{14}$ bulk metallic glass and its crystalline counterparts examined are spontaneously passivated by anodic polarization with the passive current density of about 10^{-2} A/m^2 in simulated body fluid. The higher corrosion resistance for the Ti-base bulk

metallic glass and its partial nano-crystalline alloys is attributed to stable and protective passive films.

The combination application of hydrothermal-electrochemical and pre-calcification treatments on the $Ti_{40}Zr_{10}Cu_{36}Pd_{14}$ metallic glass dramatically accelerates the nucleation and growth rates of apatite in Hanks' solution. The hydrothermal-electrochemical treatment makes a much larger surface area, increases the thickness of titanium oxide and titanium concentration on the surface of the $Ti_{40}Zr_{10}Cu_{36}Pd_{14}$ metallic glass. The micro-porous and network surface leads to much more adsorption of HPO_4^{2-} or/and Ca^{2+} ions stimulating the nucleation of calcium phosphate layer on the $Ti_{40}Zr_{10}Cu_{36}Pd_{14}$ metallic glass followed by immersion in Hanks' solution. Apatite layer can be formed quickly for only several days through two-step treatment.

Owing to the simultaneous achievement of low Young's modulus, high strength and large plastic strain, as well as good bioactivity, the Ni-free Ti-Zr-Cu-Pd-(Nb) bulk metallic glass composites are potential candidates for biomaterials. It makes it possible to apply Ti-based bulk metallic glasses with excellent properties as novel biomedical metallic implants.

5. Acknowledgement

This work is financially supported by Advanced Materials Development and Integration of Novel Structured Metallic and Inorganic Materials, Institute for Materials Research, Tohoku University.

6. References

Alvarez, M.G.; Vazquez, S.M.; Audebert, F. & Sirkin. H. (1998). Corrosion behaviour of Ni-B-Sn amorphous alloys. *Scrip. Mater*. 39, pp. 661-664

Dasa, K.; Bandyopadhyay, A. & Gupta, Y. M. (2005). Effect of crystallization on the mechanical properties of $Zr_{56.7}Cu_{15.3}Ni_{12.5}Nb_{5.0}Al_{10.0}Y_{0.5}$ bulk amorphous alloy. *Mater. Sci. Eng. A*, 394, pp. 302-311

Feng, B.; Chen, J.Y.; Qi, S.K.; He, L.; Zhao, J.Z. & Zhang, X.D. (2002). Carbonate apatite coating on titanium induced rapidly by precalcification. *Biomaterials*, 23, pp. 173-179

Healy, K.E. & Ducheyne, P. (1992). Hydration and preferential molecular adsorption on titanium *in vitro*. *Biomaterials*, 13, pp. 553-561

Heuer, A.H.; Fink, D.J.; Laraia, V.J.; Arias. J.L.; Calvert, P.D.; Kendall, K.; Messing, G.L.; Blackwell, J.; Rieke, P.C.; Thompson, D.H.; Wheeler, A.P.; Veis, A. & Calpan, A.I.; (1992). Innovative materials processing strategies: a biomimetic approach. *Science*, 255, pp. 1098-1105

Inoue, A. (1995). High strength bulk amorphous alloys with low critical cooling rates, *Mater. Trans. JIM*, 36, pp. 866-875

Inoue, A. (2000). Stabilization of metallic supercooled liquid and bulk amorphous alloys. Acta Materialia, 48, pp. 279-306

Jiang, J. Z.; Saida, J.; Kato, H. & Inoue, A. (2003). Is $Cu_{60}Ti_{10}Zr_{30}$ a bulk glass-forming alloy. *Appl. Phys. Lett.*, 82, pp. 4041-4042

Lűtjering, G. (1999). Property optimization through microstructural control in titanium and aluminum alloys. *Mater. Sci. Eng. A*, 263, pp. 117-126

Mehmood, M.; Zhang, B.P.; Akiyama E.; Habazaki, H.; Kawashina, A.; Asami, K. & Hashimoto, K. (1998). Experimental evidence for the critical size of heterogeneity areas for pitting corrosion of Cr-Zr alloys in 6 M HCl. *Corro. Sci*. 40, pp.1-17

Mondal, K.; Murty, B.S. & Chatterjee, U.K. (2005). Electrochemical behaviour of amorphous and nanoquasicrystalline Zr–Pd and Zr–Pt alloys in different environments. *Corro. Sci*. 47, pp. 2619-2635

Shukla, A.K. & Balasubramaniam, R. (2006). Effect of surface treatment on electrochemical behavior of CP Ti, Ti–6Al–4V and Ti–13Nb–13Zr alloys in simulated human body fluid. *Corro. Sci*. 48, pp. 1696-1720

Xing, L.Q.; Bertrand, C.; Dallas, J.P. & Cornet, M. (1998). Nanocrystal evolution in bulk amorphous $Zr_{57}Cu_{20}Al_{10}Ni_8Ti_5$ alloy and its mechanical properties. *Mater. Sci. Eng. A*, 241, pp. 216-225

Yang, X.J.; Hu, R.X.; Zhu. S.L.; Li, C.Y.; Chen, M.F.; Zhang, L.Y. & Cui, Z.D. (2006). Accelerating the formation of a calcium phosphate layer on NiTi alloy by chemical treatments. *Scrip. Mater*. 54, pp. 1457-1480

Biomedical Engineering, Trends in Materials Science

Edited by Mr Anthony Laskovski

ISBN 978-953-307-513-6
Hard cover, 564 pages
Publisher InTech
Published online 08, January, 2011
Published in print edition January, 2011

Rapid technological developments in the last century have brought the field of biomedical engineering into a totally new realm. Breakthroughs in materials science, imaging, electronics and, more recently, the information age have improved our understanding of the human body. As a result, the field of biomedical engineering is thriving, with innovations that aim to improve the quality and reduce the cost of medical care. This book is the second in a series of three that will present recent trends in biomedical engineering, with a particular focus on materials science in biomedical engineering, including developments in alloys, nanomaterials and polymer technologies.

InTech Europe
University Campus STeP Ri
Slavka Krautzeka 83/A
51000 Rijeka, Croatia
Phone: +385 (51) 770 447
Fax: +385 (51) 686 166
www.intechopen.com

InTech China
Unit 405, Office Block, Hotel Equatorial Shanghai
No.65, Yan An Road (West), Shanghai, 200040, China
中国上海市延安西路65号上海国际贵都大饭店办公楼405单元
Phone: +86-21-62489820
Fax: +86-21-62489821

IntechOpen